technologies

MDPI

Article

Mechanical and Tribological Properties of FFF-Printed TPU 95A with Uniform and Step-Gradient Infill Architectures

Andrey P. Vasilev *, Igor S. Makarov and Aitalina A. Okhlopkova

Department of Chemistry, North-Eastern Federal University, 58 Belinskogo St., Yakutsk 677000, Russia
* Correspondence: gtvap@mail.ru; Tel.: +7-924-869-4792

Abstract

This study evaluated the effects of uniform and symmetric step-gradient infill architectures on the density, mechanical properties, Shore D hardness, and dry-sliding coefficient of friction of FFF-printed thermoplastic polyurethane (TPU) 95A. Uniform triangular infills at 50%, 70%, and 90% were compared with a surface-dense architecture (GI-1: 90–70–50–70–90%) and a core-dense architecture (GI-2: 50–70–90–70–50%). The experimental density of GI-2 (0.988 g/cm^3) did not differ significantly from that of the uniform 70% configuration (0.990 g/cm^3). GI-2 nevertheless exhibited significantly higher tensile strength (20.3 vs. 18.4 MPa) and a higher work of deformation to failure (48.3 vs. 32.3 MJ/m^3). GI-1 had a lower experimental density than the uniform 90% configuration yet higher tensile strength and work of deformation to failure; the two configurations were not density-matched. Both gradient architectures exhibited lower mean compressive stresses at 20% strain than the uniform 70% and 90% specimens. GI-1 displayed a Shore D hardness comparable to the uniform 90% configuration and the lowest mean coefficient of friction (0.50 ± 0.01). Overall, step-gradient infill can improve specific tensile properties while allowing compressive compliance and the contact response of the outer shell to be tailored separately. However, the effects of gradient order and material content could not be fully separated because GI-1 and GI-2 differed in nominal mean infill density.

Keywords: thermoplastic polyurethane; fused filament fabrication; additive manufacturing; gradient infill; mechanical properties; coefficient of friction; hardness

1. Introduction

Additive manufacturing (AM) has been widely adopted due to its technological flexibility, high productivity in fabricating parts with complex geometries, and the ability to precisely control mechanical properties through structural design and the optimization of process parameters [1,2]. Thermoplastic polyurethane (TPU) is one of the most promising materials for additive manufacturing, owing to its combination of high elasticity, strength, wear resistance, chemical resistance, and excellent damping properties [2–4]. The fused filament fabrication (FFF) method—also known as Fused Deposition Modeling (FDM) and classified as a material extrusion (MEX) technology—enables the production of complex flexible parts from TPU, such as seals, prosthetic and orthotic components, footwear parts, damping elements, and medical devices, particularly in cases where customized geometry or a specified internal structure is required [4,5]. However, the mechanical properties of TPU parts produced by FFF are generally inferior to those of parts manufactured by injection molding or extrusion. This is due to pronounced anisotropy, incomplete fusion between filaments and layers, and the presence of voids and other defects at interlayer

Check for updates

Academic Editor: Dennis Douroumis

Received: 25 July 2026
Revised: 28 August 2026
Accepted: 28 August 2026
Published: 29 August 2026

Copyright: © 2026 by the authors. Licensee MDPI, Basel, Switzerland. This article is an open access article distributed under the terms and conditions of the Creative Commons Attribution (CC BY) license.

boundaries [6,7]. Experimental studies of the tensile properties of FFF-printed specimens made of TPU 95A also confirm that printing parameters and specimen orientation significantly affect the strength and deformation behavior of the material [8].

The mechanical properties of polymer parts fabricated by FFF depend not only on the feedstock material but also, to a large extent, on processing parameters such as layer thickness, infill angle, infill density, printing speed, and nozzle temperature. For TPU, these parameters are particularly critical, as variations in printing temperature, printing speed, layer height, and infill strategy determine not only the tensile strength and elongation at break, but also the overall fracture behavior and interlayer bonding quality [4,9–13]. In this context, perimeter lines are critical to part integrity, especially when using unidirectional infill patterns. These observations indicate that the mechanical behavior of FFF elastomers is governed not only by the bulk material density but also by the spatial arrangement of filaments, perimeters, and internal infill regions.

Numerous studies emphasize the critical role of infill pattern and density in shaping the mechanical behavior of FFF-printed TPU parts [14–17]. In particular, compressive stress has been shown to increase with increasing infill density; however, deformation behavior is largely determined by the specific spatial architecture [18]. Three-dimensional lattice structures, such as gyroid and cubic architectures, exhibit more predictable and stable behavior compared to two-dimensional patterns, which may be more susceptible to strain localization, delamination, and unstable failure in interlayer regions [18,19]. Consequently, for FFF-printed TPU parts, it becomes important not only to select the nominal infill density but also to control the spatial distribution of material within the specimen volume.

One of the most promising approaches to tailoring the properties of FFF-printed parts is the use of functionally graded structures, in which the infill density varies along the height or another spatial direction [20–22]. In contrast to uniform infill, gradient architectures allow for the efficient redistribution of material within the part without significantly increasing its average density [23]. This enables local tailoring of component stiffness, deformability, energy absorption capacity, and contact compliance. For elastomeric materials such as TPU, this approach is particularly relevant, since their functional performance depends not only on the overall material fraction but also on the spatial arrangement of denser and more compliant zones within the part volume.

For many practical applications of TPU-based components, both bulk mechanical performance (strength and deformability) and surface behavior under contact and friction are equally critical [24]. In FFF-printed parts, the architecture of the subsurface infill may affect the support and effective contact compliance of the solid outer shell and, consequently, its indentation and frictional response [25–27]. Structures with similar bulk densities but different subsurface and core arrangements may then show different mechanical, contact and tribological responses.

Unlike earlier studies that treated graded structures as a single class, we compare two symmetric step-gradient configurations built from the same local infill levels (50%, 70% and 90%) but arranged in inverse surface-dense and core-dense sequences. They are not matched in nominal mean infill density and should not be read as an isolated test of gradient order. We therefore focus on GI-2 versus the uniform 70% configuration, for which no statistically significant difference in experimental bulk density was detected.

Most previous studies of graded TPU structures have focused on the compressive behavior and energy absorption of honeycomb, cellular or lattice geometries. Here, we examine solid-shell FFF specimens with a conventional triangular infill whose density changes in five discrete steps along the printer *Z*-axis. In addition to tensile and compressive behavior, experimental density, Shore D hardness and dry-sliding friction were measured in order to link bulk mechanical performance with surface-supported contact properties.

The contribution is a combined assessment of through-thickness step-gradient triangular infill, not of functionally graded TPU as a general concept.

The aim of this work is to compare the density, tensile and compressive response, Shore D hardness and dry-sliding friction of FFF-printed TPU 95A specimens with uniform triangular infill and two symmetric step-gradient architectures. The specific question was whether a surface-dense arrangement (GI-1) and a core-dense arrangement (GI-2) produce different combinations of bulk and contact properties relative to uniform structures.

2. Materials and Methods

2.1. Material and Specimen Preparation

Commercial transparent Easy Flex 95A thermoplastic polyurethane filament manufactured by REC (Moscow, Russia) was used. The filament diameter was 1.75 mm, the nominal material density was 1.15 g/cm^3, and the specified operating temperature range was –35 °C to +80 °C.

Before printing, the TPU was dried in a drying oven at 70 °C for 4 h to remove moisture. All printed specimens were conditioned at a temperature of 23 ± 2 °C and a relative humidity of 50 ± 5% for at least 48 h prior to testing, in accordance with ISO 291:2008 [28]. Three-dimensional specimen models were designed in KOMPAS-3D version 23 (ASCON, St. Petersburg, Russia) and exported in STL format. G-code preparation (slicing) was performed using Ultimaker Cura version 5.9.1. The specimens were fabricated by fused filament fabrication (FFF) on a Creality Ender 3 S1 Pro 3D printer (Creality, Shenzhen, China). The fixed 3D printing process parameters are listed in Table 1.

Table 1. Fixed 3D printing parameters.

Parameter	Value
Nozzle diameter, mm	0.4
Layer height, mm	0.2
Nozzle temperature, °C	225
Bed temperature, °C	35
Printing speed, mm/s	60
Top and bottom layer thickness, mm	0.4 (2 layers of 0.2 mm each)
Number of perimeters (walls)	2 (width 0.4 mm)

The principal variables were the infill density and its spatial distribution along the printer *Z*-axis. The printer coordinate system was defined as follows: the build plate was parallel to the XY plane, and the layer-stacking or build direction was parallel to the *Z*-axis. Individual layers were deposited in planes parallel to the XY plane. All specimens were printed using a triangular infill pattern, two solid top layers, two solid bottom layers, and two perimeter walls.

For the control specimens, uniform infill densities of 50%, 70%, and 90% were applied. These values were selected as representative low, intermediate, and high infill levels that can be directly specified using the standard FFF slicing procedure. The nominal Infill Density parameter is not equivalent to the experimental density of a printed specimen because the latter also includes the contributions of the solid outer shell and perimeters and is affected by interfilament voids and other FFF-related defects. Therefore, the gradient structures were compared with the uniform structures using both nominal infill density and experimentally measured density.

Step-gradient infill was generated in Ultimaker Cura version 5.9.1 using “Per Model Settings” modifiers. Each modifier covered the entire specimen cross-section in the XY plane and defined the infill density within a specified interval along the printer *Z*-axis.

Thus, the gradient direction coincided with the build and layer-stacking direction and was perpendicular to the deposited-layer planes. The total height of each specimen along the *Z*-axis was divided into five equal zones, each having a thickness of $h/5$, where h is the total specimen dimension along the *Z*-axis. All five zones had the same nominal thickness along Z. With the triangular infill pattern kept unchanged, infill-density sequences of 90–70–50–70–90% and 50–70–90–70–50% were assigned from the bottom, build-plate-side surface to the top surface for GI-1 and GI-2, respectively. Because the five zones had equal nominal dimensions along the *Z*-axis, the nominal mean infill density was determined as the arithmetic mean of the five specified Infill Density values. For GI-1, the nominal mean infill density was:

$$\text{Infill}_{\text{GI}-1} = \frac{90 + 70 + 50 + 70 + 90}{5} = 74\%, \quad (1)$$

For GI-2, the nominal mean infill density was

$$\text{Infill}_{\text{GI}-2} = \frac{50 + 70 + 90 + 70 + 50}{5} = 66\%, \quad (2)$$

The layer ranges for the five equal-thickness gradient zones were as follows:

- Tensile specimens (3.8 mm, 19 layers): layers 3–5, 6–8, 9–11, 12–14 and 15–17;
- Compression specimens (25.8 mm, 129 layers): layers 3–27, 28–52, 53–77, 78–102 and 103–127;
- Friction and density specimens (5.8 mm, 29 layers): layers 3–7, 8–12, 13–17, 18–22 and 23–27;
- Solid bottom layers 1–2 and solid top layers were excluded from the gradient in all cases.

The parameters of the uniform and gradient TPU specimens are summarized in Table 2.

Table 2. Infill parameters of TPU specimens.

Configuration	Designation	Infill Density Sequence (Bottom to Top)	Nominal Mean Infill Density, %	Infill Pattern	Implementation Method
Uniform infill	50%	50%	50	Triangular	Standard Cura infill
Uniform infill	70%	70%	70	Triangular	Standard Cura infill
Uniform infill	90%	90%	90	Triangular	Standard Cura infill
Surface-dense gradient	GI-1	90% → 70% → 50% → 70% → 90%	74	Triangular	Per Model Settings infill modifiers
Core-dense gradient	GI-2	50% → 70% → 90% → 70% → 50%	66	Triangular	Per Model Settings infill modifiers

Note: The sequences are reported along the printer *Z*-axis from the build-plate-side surface to the top printed surface. "Surface-dense" refers to the top and bottom surfaces (normal to the build direction).

A schematic representation of the gradient profiles, including the arrangement of the modifiers, is shown in Figure 1. The gradient profiles were verified in the Layer View preview mode with the infill display enabled.

Tensile specimens with Type IV geometry based on ASTM D638-22 [29] were used; the thickness was set to 3.8 mm to obtain an integer number of 0.2 mm layers. The specimens were printed flat on the build plate, with their longitudinal axis parallel to the printer *X*-axis, width direction parallel to the *Y*-axis, and thickness direction parallel to the *Z*-axis. Consequently, the five gradient zones were distributed through the specimen thickness along the *Z*-axis. The infill-gradient direction was perpendicular to the longitudinal axis of the specimen and to the subsequent tensile-loading direction. The deposited-layer planes lay in XY and contained the tensile axis.

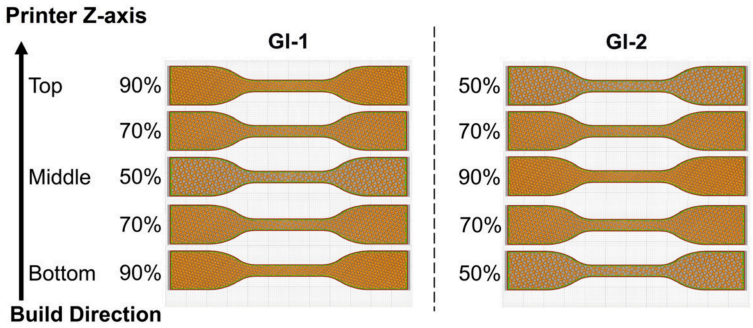

Figure 1. Schematic representation of the uniform and step-gradient infill profiles along the printer *Z*-axis, from the build-plate-side surface to the top printed surface: uniform 50%, 70%, and 90% configurations and gradient GI-1 and GI-2 configurations. Each gradient zone had the same dimension along the *Z*-axis.

Cylindrical compression specimens based on ASTM D695-23 [30] were used; the height was set to 25.8 mm for the same reason. The cylinders were printed vertically, with their longitudinal axes parallel to the printer *Z*-axis. Consequently, the five gradient zones were distributed along the cylinder height. The infill-gradient, cylinder-axis, build, and subsequent compression-loading directions were mutually parallel and perpendicular to the deposited layers.

The specimen dimensions and orientations relative to the printer coordinate system are shown in Figure 2. For each infill configuration, five specimens were manufactured for tensile testing and five specimens for compression testing.

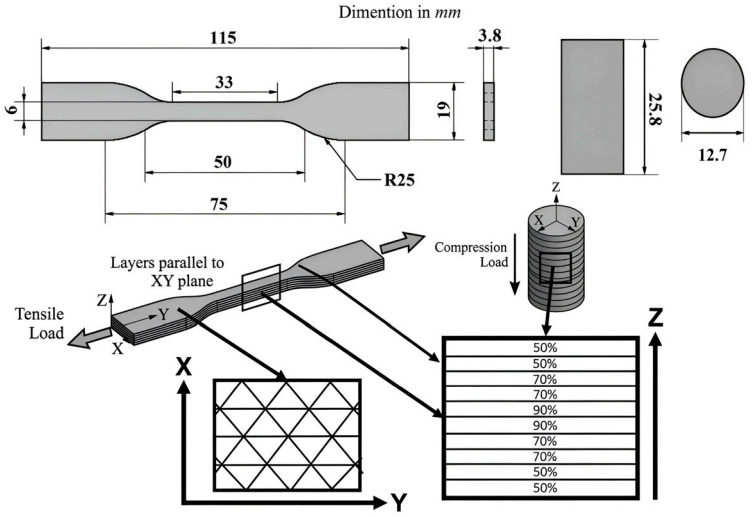

Figure 2. Dimensions and orientations of the TPU 95A specimens relative to the printer coordinate system. Arrows indicate the printer axes (X, Y, Z) and the loading direction. The tensile specimen was printed flat, with the tensile axis parallel to X and the infill gradient through the thickness (Z). The cylindrical compression specimen was printed vertically, with the cylinder axis, build direction, infill gradient and compression axis parallel to Z. In both cases, the deposited layers were parallel to the XY plane.

2.2. Material Characterization Methods

The chemical structure of the TPU specimens was characterized by Fourier-transform infrared (FTIR) using a Varian 7000 FT-IR spectrometer (Varian, Palo Alto, CA, USA) equipped with an ATR accessory. The spectra were recorded in the range of 550–4000 cm^{-1}.

Thermal transitions were characterized by differential scanning calorimetry (DSC) using a DSC 204F1 Phoenix system (Netzsch, Selb, Germany). Samples weighing 13–15 mg

were placed in aluminum crucibles, held at 40 °C for 10 min, and then heated to 250 °C at a rate of 10 °C/min under a helium flow. The analysis was performed on the first heating cycle, which allowed assessment of the thermal state of the material as formed during the FFF printing process. The temperatures of endothermic transitions were determined from the corresponding peak maxima.

Morphological features of the specimens were examined using a JEOL JSM-7800F scanning electron microscope (SEM; JEOL, Tokyo, Japan). No conductive coating was applied to the specimen surfaces. To prevent static charge accumulation and reduce charging artifacts, imaging was performed at a low accelerating voltage of 1–2 kV using a secondary electron detector.

2.3. Mechanical Testing

Tensile and compression tests were performed using an Autograph AGS-J universal testing machine (Shimadzu, Kyoto, Japan). The loading orientations relative to the printer coordinate system are shown in Figure 2. Tensile loading was applied along the longitudinal axis of the dog-bone specimen, parallel to the printer *X*-axis and perpendicular to the *Z*-directed infill gradient. Thus, the five infill-density zones located through the specimen thickness were subjected simultaneously to longitudinal tensile loading. Compression was applied along the longitudinal axis of the cylindrical specimen, parallel to the printer *Z*-axis. Consequently, the compression-loading direction was parallel to the infill-gradient and build directions and perpendicular to the deposited-layer planes. The tensile-test crosshead speed of 500 mm/min was selected from the test speeds specified in ASTM D638-22 for materials expected to exhibit elongation greater than 100%. This speed was selected before testing based on the highly extensible behavior expected for TPU 95A and was applied consistently to all configurations. A compression-test crosshead speed of 2 mm/min was selected from the test speeds specified in ASTM D695-23. The gauge length was 25 mm. No specimen slippage was observed during tensile testing, as verified by reference marks made adjacent to the grips. In both cases, strain was determined from crosshead displacement due to the absence of an extensometer capable of tracking elongation above 300%. While this may lead to a slight overestimation of absolute strain values, the relative differences between configurations remain reliable, as all specimens were tested under identical conditions. The work of deformation to failure, W, was calculated as the area under the engineering stress–strain curve up to specimen failure (equivalent to tensile toughness, or strain energy density to failure):

$$W = \int_0^{\varepsilon_b} \sigma(\varepsilon) d\varepsilon, \tag{3}$$

where ε_b is the strain at break. Compression tests were conducted up to a relative strain of at least 20%, and the compressive stress was analyzed at ε = 5, 10, and 20%. The results are reported as the mean ± standard deviation.

To evaluate the material utilization efficiency, the specific tensile strength was calculated using the following formula:

$$\sigma_{sp} = \frac{\sigma_{UTS}}{\rho_{exp}}, \tag{4}$$

where σ_{UTS} is the tensile strength, MPa; ρ_{exp} is the experimental density of the specimen, g/cm^3. The value of σ_{sp} is expressed in MPa·cm^3/g.

The specific work of deformation to failure, W_{sp}, was calculated as

$$W_{sp} = \frac{W}{\rho_{exp}}, \tag{5}$$

where W is the work of deformation to failure, MJ/m^3, and ρ_{exp} is the experimental bulk density, g/cm^3. With these units, W_{sp} is expressed in kJ/kg.

2.4. Friction Testing

The frictional behavior of the TPU 95A specimens was investigated using a ball-on-disk configuration under dry sliding conditions on a UMT-3 testing machine (CETR, Mountain View, CA, USA) at room temperature. An AISI E52100 chromium-steel ball with a diameter of 6.5 mm and a hardness of 63 HRC was used as the counterbody. The sliding-track radius was 25 mm. The tests were conducted under a normal load of 5 N, at a sliding speed of 150 mm/s, and over a total sliding distance of 300 m. Three independently printed specimens were tested for each infill configuration. The dimensions of the specimens for friction testing are shown in Figure 3.

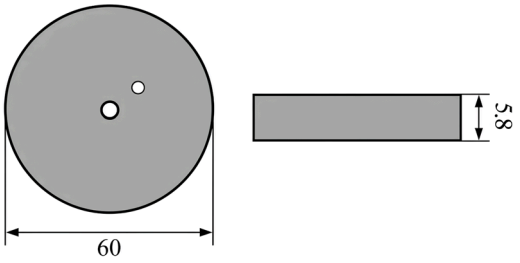

Figure 3. Dimensions of specimens for friction testing.

The coefficient of friction was continuously recorded over the complete sliding distance from 0 to 300 m. For quantitative comparison, the mean COF over the final sliding-distance interval from 250 to 300 m was calculated separately for each specimen. This interval was selected as a consistent late-stage comparison window after most of the initial friction evolution had occurred. Because a gradual increase in COF remained visible over the sliding distance for some configurations, this interval was not interpreted as a fully established steady-state regime. The resulting specimen-level values are reported as the mean ± standard deviation. Individual time points within a friction curve were not treated as independent observations.

The ball-on-disk experiments were designed to quantify dry-sliding frictional behavior rather than wear resistance. Preliminary contact profilometry and optical microscopy were evaluated for quantitative characterization of the sliding tracks but did not yield sufficiently reliable data for the compliant, rough, and optically transparent TPU specimens (see Section 3.5 for details). Consequently, no track depth, cross-sectional area, or wear volume was calculated. SEM was used only for qualitative characterization of the post-sliding surface morphology.

2.5. Density, Apparent Porosity, and Hardness Measurements

The experimental density was determined by hydrostatic weighing from the specimen masses measured in air and in distilled water, in accordance with Russian Standard GOST 15139-69 [31] at room temperature (23 ± 2 °C). Density was measured using separate rectangular specimens with dimensions of 30 × 30 × 5.8 mm, printed with the same infill configurations and parameters as the mechanical test specimens. This geometry provided sufficient volume for reliable hydrostatic weighing while avoiding the irregular shape of the dog-bone specimens, which could introduce errors due to entrapped air in the gauge section during immersion. Five specimens were tested for each infill configuration. Distilled water was used as the working fluid. Before each measurement, the specimens were conditioned in the laboratory environment for at least 24 h to achieve moisture equilibrium. The mass in air was recorded prior to immersion, after which the specimen was fully

submerged in water, with any visible air bubbles carefully removed from its surface using a soft brush. The density value was calculated as the arithmetic mean of five specimens for each configuration.

The relative density was calculated using the following formula:

$$\rho_{\text{rel}} = \frac{\rho_{\text{exp}}}{\rho_{\text{TPU}}} \cdot 100\%, \quad (6)$$

where ρ_{exp} is the experimental density of the printed specimen, and ρ_{TPU} is the nominal density of the pristine TPU.

The apparent porosity was calculated as

$$P = 100\% - \rho_{rel}, \quad (7)$$

The hardness of the printed specimens was measured at room temperature using an analog durometer TBP-D (Vostok-7, Moscow, Russia) on the Shore D scale in accordance with ISO 868:2003 [32]. Shore D hardness was measured on the top-printed surface of the specimens. Each specimen had a total thickness of 5.8 mm, including a 0.4 mm solid top layer, and was placed on a flat rigid support during measurement. The durometer was applied perpendicular to the surface without impact, and the maximum reading indicated by the peak-holding pointer was recorded. One measurement was taken per independently printed specimen, and five specimens were tested for each configuration. The specimen-level values were used as independent observations in the statistical analysis (n = 5 specimens per configuration). Shore D hardness represents the indentation response of the tested specimen rather than an intrinsic hardness value of the 0.4 mm solid top layer considered separately. Accordingly, specimens with identical nominal outer-layer thicknesses may exhibit different Shore D values when their outer layers are supported by subsurface regions with different structural compliance.

2.6. Statistical Analysis

Statistical processing of the results of density, hardness, and mechanical property determinations was performed using one-way analysis of variance (ANOVA) followed by Tukey's HSD test for multiple pairwise comparisons. The data are presented as the mean ± standard deviation. For mechanical testing, density determination, and hardness measurements, n = 5 was used. Differences were considered statistically significant at $p < 0.05$. For friction testing, n = 3 independently printed specimens were used per configuration. Late-stage COF values were compared descriptively and were not analyzed by ANOVA.

3. Results and Discussion

3.1. Thermal and Spectroscopic Characteristics of TPU

To assess the possible influence of FFF printing on the thermal state and chemical structure of TPU, the pristine filament and printed specimens were investigated. Because no substantial differences were observed among the infill configurations, representative DSC curves and FTIR spectra are presented in Figure 4.

The DSC curve of the pristine filament showed a low-temperature endothermic peak at approximately 85 °C, whereas the corresponding peaks of the printed specimens occurred at 69–71 °C. This transition may be associated with the melting of poorly ordered domains and the relaxation of physical bonds in the soft segments of TPU [33]. In the high-temperature region, endothermic maxima were recorded at 182–196 °C, consistent with the melting of ordered hard segments and crystalline or pseudocrystalline domains of TPU [34,35]. The

slight differences between the filament and the printed specimens can plausibly be linked to the thermal history of the material during extrusion and layer cooling, as well as changes in the degree of microphase separation of hard and soft segments [33,36].

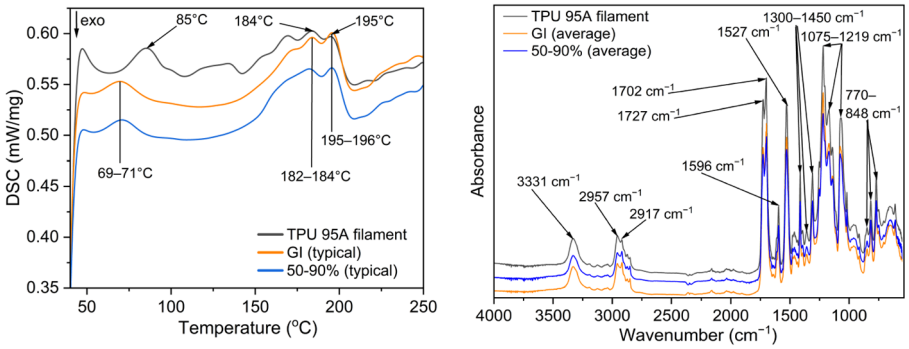

Figure 4. Typical DSC curves (**a**) and FTIR spectra (**b**) of the pristine TPU filament and FFF-printed TPU 95A specimens.

The FTIR spectra of all investigated specimens were similar (Figure 4b). The band at 3331 cm^{-1} corresponds to stretching vibrations of N–H groups involved in hydrogen bonding, while the bands at 2957 and 2917 cm^{-1} can be assigned to C–H stretching vibrations in the methylene groups of the soft segments [37,38]. In the carbonyl region, bands were observed at 1727 cm^{-1} and 1702 cm^{-1}, corresponding to free and hydrogen-bonded carbonyl groups, respectively [39,40]. The band at 1527 cm^{-1} belongs to the amide II region, involving N–H bending and C–N stretching vibrations of the urethane group [40–42], while the intense bands in the range of 1075–1219 cm^{-1} are attributed to C–O and C–O–C vibrations of the polyurethane moieties [41,43].

The combined DSC and FTIR data suggest that the observed differences are most likely related to changes in the thermal history and supramolecular organization of the material. No pronounced signs of chemical degradation within the sensitivity limits of the methods used were detected.

3.2. Experimental Density and Apparent Porosity

Table 3 presents the experimental density, relative density, and apparent porosity of the specimens with uniform and gradient infill.

Table 3. Experimental density and apparent porosity of TPU 95A specimens.

Configuration	Nominal Mean Infill Density, %	ρ_{exp}, g/cm^3	ρ_{rel}, %	P, %
Uniform 50% infill	50	0.860 ± 0.016	74.8	25.2
Uniform 70% infill	70	0.990 ± 0.016	86.1	13.9
Uniform 90% infill	90	1.090 ± 0.022	94.8	5.2
GI-1	74	1.028 ± 0.019	89.4	10.6
GI-2	66	0.988 ± 0.026	85.9	14.1

As the uniform infill increased from 50 to 90%, the experimental density increased from 0.860 to 1.090 g/cm^3, while the apparent porosity decreased from 25.2 to 5.2% (Table 3). The density of GI-2 was 0.988 g/cm^3, comparable to the uniform 70% configuration, whereas GI-1 exhibited intermediate values between the uniform 70% and 90% configurations. Statistical comparison using one-way ANOVA with Tukey's HSD post hoc test indicated that the density difference between GI-2 and uniform 70% was not significant (p = 0.9999).

Individual density measurements and the complete statistical results are provided in Supplementary Tables S7–S9.

Slicer-defined infill density deviates from experimental values. This discrepancy arises because the software parameter omits solid shell contributions, microscopic gaps, and fabrication flaws inherent to FFF [44–46]. Thus, at a nominal infill of 50%, the relative density of the specimen reached 74.8%.

Similarly, the nominal mean infill densities of the gradient specimens—74% for GI-1 and 66% for GI-2—were lower than their experimental relative densities of 89.4% and 85.9%, respectively, because of the contributions of the solid outer layers and perimeters. Nevertheless, the effects of architecture and material content cannot be completely separated when GI-1 and GI-2 are compared because these configurations differ in both the arrangement and volumetric proportions of the dense and sparse zones.

Mechanical comparisons therefore center on GI-2 and the uniform 70% configuration. These configurations had very similar mean experimental densities (0.988 and 0.990 g/cm^3), and no statistically significant density difference was detected; this result does not demonstrate statistical equivalence.

3.3. Tensile and Compressive Behavior

Figure 5 presents the tensile strength, elongation at break, work of deformation to failure and compressive stresses at relative strains of 5, 10, and 20% for TPU 95A specimens with uniform and gradient infill.

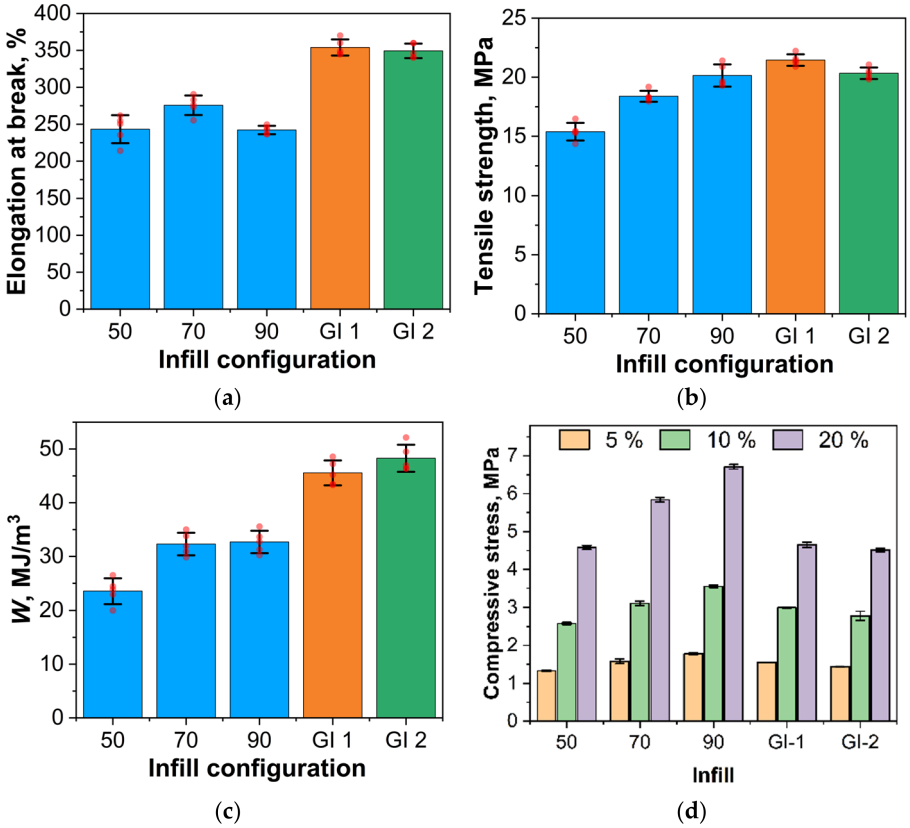

Figure 5. Mechanical characteristics of TPU 95A specimens with uniform and gradient infill: elongation at break (**a**), tensile strength (**b**), work of deformation to failure (**c**), and compressive stress at strain 5%, 10%, and 20% (**d**). Red circles show independently printed and tested specimens; bars and error bars denote the mean ± specimen standard deviation (n = 5 specimens per configuration).

3.3.1. Tensile Behavior and Specific Mechanical Properties

The GI-1 and GI-2 specimens exhibited elongations at break of 354% and 349%, respectively, exceeding the range measured for the uniform configurations of 243–276% (Figure 5a). The tensile strength of the uniform specimens increased from 15.4 MPa at 50% infill to 20.1 MPa at 90% infill. The mean tensile strengths of GI-1 and GI-2 were 21.5 and 20.3 MPa, respectively. At the same time, the strength of GI-1 was significantly higher than that of the uniform 90% configuration (p = 0.0345), despite the lower experimental density of GI-1. Meanwhile, GI-2 exceeded the strength of the uniform 70% configuration by 10.6% (20.3 ± 0.5 vs. 18.4 ± 0.4 MPa, p = 0.0011), even though these specimens had comparable experimental density.

Thus, the gradient architecture produces a simultaneous increase in both strength and deformability. This finding is consistent with published data showing that the mechanical response of FFF-printed TPU specimens depends not only on the total amount of material but also on the spatial arrangement of filaments, perimeters and internal infill zones [11,13,16,17].

The mean work of deformation to failure of the uniform specimens increased from 23.55 MJ/m^3 at 50% infill to 32.3 MJ/m^3 at 70% infill and remained similar at 32.7 MJ/m^3 for the 90% configuration. No statistically significant difference was detected between the uniform 70% and 90% configurations (p = 0.9988). The corresponding values for GI-1 and GI-2 were 45.6 and 48.3 MJ/m^3, respectively, and did not differ significantly from each other (p = 0.3561). Relative to the uniform 70% configuration, the mean work of deformation to failure of GI-2 was 49.4% higher (p < 0.001). Relative to the uniform 90% configuration, the mean value for GI-1 was 39.3% higher (p < 0.001), despite the lower experimental density of GI-1. Given the density comparison in Section 3.2, these increases are consistent with a contribution of spatial infill architecture to the tensile response. However, the macroscopic differences do not identify the local damage or strain-redistribution mechanisms responsible for the improvement.

To compare the material utilization efficiency, the specific strength σ_{sp} and the specific tensile work of deformation to failure (W_{sp}) were calculated. The results are presented in Table 4.

Table 4. Specific mechanical properties of TPU 95A specimens.

Configuration	σ_{sp}, MPa·cm^3/g	W_{sp}, kJ/kg
Uniform 50% infill	17.89	27.39
Uniform 70% infill	18.57	32.63
Uniform 90% infill	18.48	30.00
GI-1	20.87	44.31
GI-2	20.58	48.87

Note: σ_{sp} and W_{sp} were calculated from the unrounded group means of tensile strength, work of deformation to failure (Supplementary Table S2), the unrounded mean experimental densities (Table 3) and were then rounded to two decimal places.

The gradient configurations exhibited higher specific work of deformation to failure than the uniform configurations. The W_{sp} values were 44.31 and 48.87 kJ/kg for GI-1 and GI-2, respectively, compared with 27.39–32.63 kJ/kg for the uniform configurations.

Both GI-1 and GI-2 retained this advantage after normalization to experimental density, indicating that the differences in tensile behavior cannot be explained by material content alone. This is most clearly demonstrated by the comparison of GI-2 with the uniform 70% configuration, which showed comparable mean experimental densities and no statistically significant difference in density. The result points to a real contribution of spatial architecture to the mechanical response. Consequently, the enhanced performance of the gradient structures is achieved without increasing material consumption, offering

a practical route to lightweight, material-efficient components that maintain or improve mechanical properties.

3.3.2. Compressive Behavior

Compressive stresses were determined at relative strains of 5, 10, and 20%. For uniform configurations, compressive stress increased with higher infill density across the entire strain range investigated. At 5 and 10% strain, GI-1 and GI-2 occupied an intermediate position between the uniform specimens, with GI-1 exhibiting slightly higher stresses. At 20% strain, the stresses of GI-1 and GI-2 were 4.6 and 4.5 MPa, respectively, and were lower than those of the 70 and 90% configurations. This trend mirrors data reported for FFF structures, according to which an increase in material fraction and a reduction in porosity enhance their compressive resistance [18,19].

The gradient configurations generally exhibited higher mean tensile strength, elongation at break, and work of deformation, together with lower compressive stresses at 20% strain than the uniform 70% and 90% configurations. Thus, they combine high extensibility with increased compressive compliance, which may be beneficial for damping and orthopedic components. Similar effects of spatial density distribution on compressive response have been reported in [21].

3.4. Fracture Morphology

Figure 6 shows SEM images of the fracture surfaces of TPU 95A specimens with uniform and gradient infill patterns.

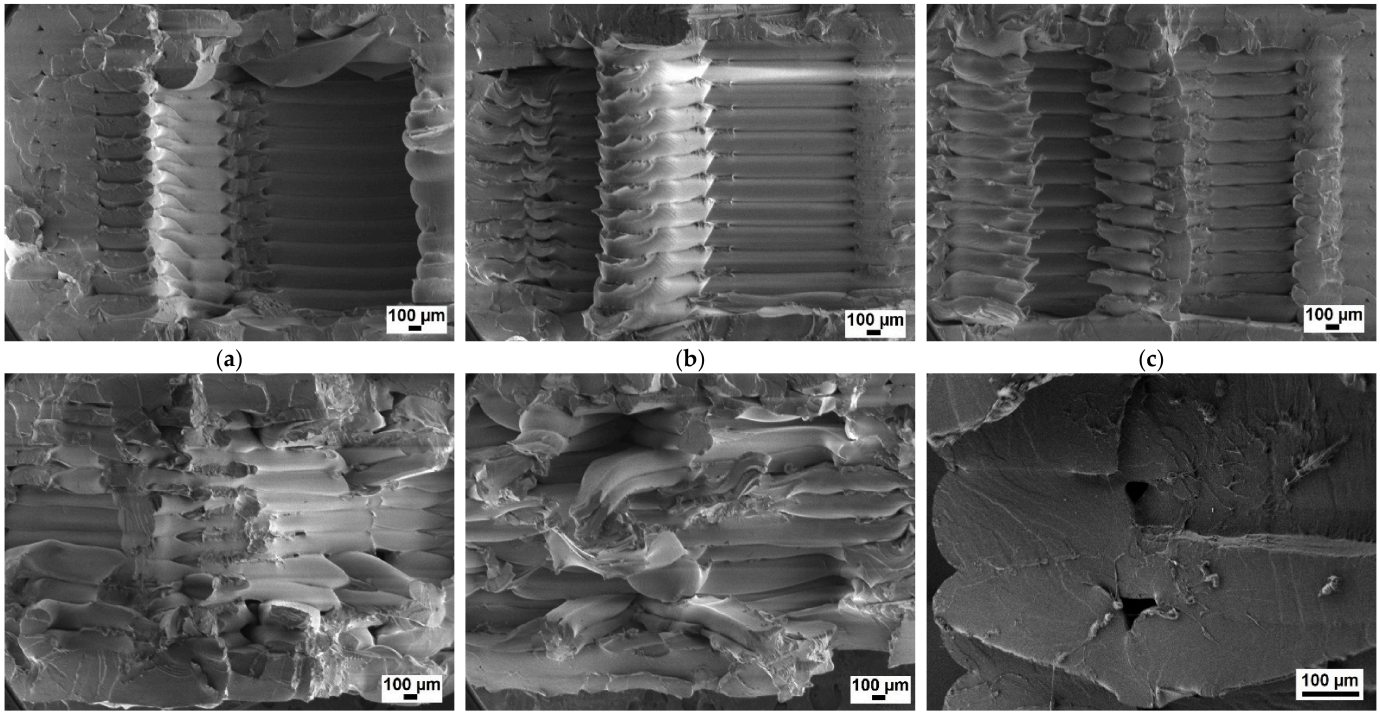

Figure 6. SEM images of fracture surfaces of TPU 95A: (**a**) 50%; (**b**) 70%; (**c**) 90%; (**d**) GI-1; (**e**) GI-2; (**f**) higher-magnification image of representative voids in GI-1.

The fracture surfaces of the specimens with uniform infill densities of 50–90% exhibited similar morphological features (Figure 6a–c). The images revealed extruded filaments and distinct interfilament boundaries. Signs of pronounced plastic drawing and crushing of the filaments were only weakly evident. For the gradient configurations, more pronounced deformation and local crushing of individual filaments were observed than for

the uniform configurations (Figure 6d,e). These post-fracture features are qualitatively consistent with the higher macroscopic elongation at break of the gradient specimens, but they do not independently establish the sequence of damage initiation and propagation. Because the infill gradient was oriented through the specimen thickness and perpendicular to the tensile-loading direction, regions with different local infill densities were loaded simultaneously. Under this orientation, damage could potentially initiate at interfilament voids, layer interfaces, specimen edges, or transitions between regions of differing local stiffness. The gradient may influence subsequent damage evolution in two opposing ways. On the one hand, the more compliant zones may promote local deformation and strain redistribution, while the denser zones may provide additional load-bearing paths and delay macroscopic separation. On the other hand, transitions between zones of different local infill density may create stiffness mismatches that act as sites of strain concentration. The post-fracture morphology is compatible with strain redistribution and progressive failure of regions with different local compliance. It does not demonstrate crack arrest, crack-tip blunting or stepwise propagation. Direct confirmation would require in situ local-strain mapping, time-resolved crack observation, three-dimensional porosity characterization, or numerical simulation. Additionally, defects typical of this manufacturing technology were observed. These took the form of rounded and triangular voids with characteristic sizes of approximately 40–60 μm (Figure 6f). Such defects may reduce the strength and stiffness of printed parts. The absence of extended slit-like defects and pronounced interlayer delamination indicates satisfactory filament fusion under the selected printing parameters [44,45].

One limitation is the absence of direct cross-sectional validation of the internal infill architecture. Optical microscopy of polished cross-sections was attempted but proved impractical due to the optical transparency of the TPU material, which caused superposition of multiple layers and prevented clear visualization of the boundaries between adjacent gradient zones. In the absence of direct cross-sectional imaging, the experimental density measurements characterize the overall material content but do not validate the spatial distribution of the local infill zones. Similarly, the observed mechanical, hardness, and frictional differences are consistent with the programmed architectures but cannot serve as independent structural validation. Direct verification of the as-printed architecture remains necessary.

3.5. Hardness and Frictional Behavior

Figure 7 presents the Shore D hardness and coefficient of friction (COF) of TPU 95A specimens with uniform and gradient infill architectures.

The Shore D hardness of the uniform specimens increased from 31.6 to 48.4 as the infill density rose from 50% to 90% (Figure 7a). This trend demonstrates that the indentation response of the printed specimens depended on their internal material fraction, even though the nominal thickness of the solid outer layer was identical in all cases. The mean hardness of GI-1 was 49.2 Shore D and did not differ significantly from that of the uniform 90% configuration ($p = 0.9554$), despite the lower experimental density of GI-1. This indicates the influence of the subsurface infill architecture on the resistance of the continuous outer shell to local indentation [47]. In contrast, GI-2 exhibited a mean hardness of 33.4 Shore D, which did not differ significantly from that of the uniform 50% configuration ($p = 0.5369$), despite the similar mean experimental densities of GI-2 and the uniform 70% specimens.

These results show that the measured Shore D hardness did not reflect the response of the 0.4 mm solid top layer in isolation. Instead, the outer shell and the subsurface infill acted as a mechanically coupled system. In GI-1, the 90% infill region immediately beneath

the solid top layer provided stiffer support and greater resistance to indentation, whereas in GI-2 the corresponding 50% subsurface region provided more compliant support.

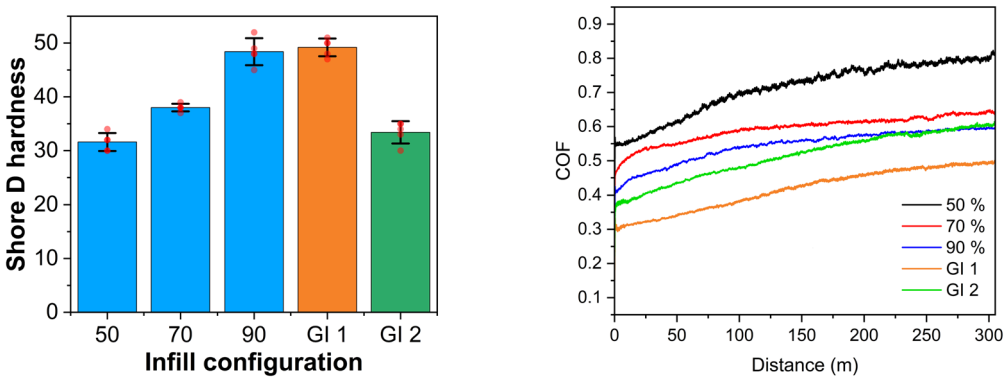

(**a**) (**b**)

Figure 7. Shore D hardness and dry-sliding frictional behavior of TPU 95A specimens with different infill architectures. (**a**) Shore D hardness: red circles show independently printed specimens; bars and error bars are the mean ± standard deviation (n = 5 specimens per configuration). (**b**) Representative coefficient-of-friction curves over the full sliding distance of 0–300 m (n = 3 specimens per configuration; one curve is shown for each configuration).

The uniform 70% configuration exhibited significantly higher hardness than both the uniform 50% and GI-2 configurations (p = 0.0057) and significantly lower hardness than the uniform 90% and GI-1 configurations ($p < 0.001$). Thus, the hardness of GI-1 was comparable to that of the uniform 90% specimens, whereas GI-2 exhibited hardness similar to the uniform 50% configuration, despite their intermediate mean densities. Overall, the hardness results indicate that the local distribution of material in the subsurface region was more important for the indentation response than the mean experimental density alone.

Figure 7b shows that the coefficient of friction gradually increased with sliding distance for all configurations, a behavior typical of elastomers under dry-sliding conditions [48,49]. Among the uniform specimens, higher infill density was associated with a lower mean COF (calculated over the 250–300 m interval), which decreased from 0.81 ± 0.02 for the 50% configuration to 0.59 ± 0.02 for the 90% configuration.

GI-1 exhibited both the lowest mean COF (0.50 ± 0.01) and the highest Shore D hardness. GI-2 produced a mean COF of 0.61 ± 0.02, placing it between the uniform 70% and 90% configurations. Because only three independently printed specimens were tested per configuration, the COF differences are interpreted descriptively rather than as statistically confirmed differences. The observed trend is consistent with the known tendency of elastomers to display lower friction coefficients as effective stiffness increases [48,50]. The lower COF of GI-1 is consistent with the lower contact compliance of the surface-dense architecture. However, Shore D hardness alone does not reveal the deformation state under the spherical contact used in the ball-on-disk test. Friction in TPU can also be influenced by adhesion, viscoelastic hysteresis, surface topography, frictional heating and running-in behavior. Consequently, the contribution of subsurface support to the observed COF differences is regarded as a plausible mechanism rather than a directly demonstrated causal relationship. Moreover, the normal indentation depth under the 5 N load with a 6.5 mm steel ball was not measured, and the tribometer displacement signal could not separate specimen indentation from machine compliance. Penetration of the contact stress field through the 0.4 mm solid outer shell therefore remains unconfirmed, and Shore D hardness (obtained with a different indenter geometry and load) cannot substitute for this measurement. Direct measurement of indentation depth under the same contact conditions will be required in future work.

Figure 8 shows SEM images of the sliding-track surfaces of TPU 95A after ball-on-disk friction testing. All specimens had the same number of solid outer layers and were printed with the same nominal outer-shell geometry. Nevertheless, differences in subsurface infill architecture may have affected the effective contact compliance and deformation of the shell under load.

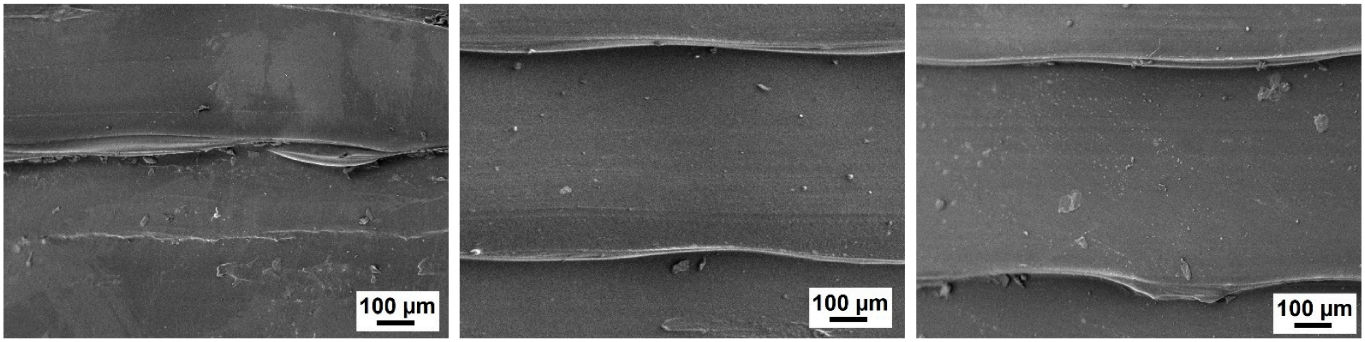

(**a**) (**b**) (**c**)

Figure 8. SEM images of the post-sliding surfaces of TPU 95A specimens after ball-on-disk testing: (**a**) uniform 90% infill; (**b**) GI-1; (**c**) GI-2.

All examined specimens exhibited local smoothing and deformation of the original as-printed surface topography within the sliding tracks (Figure 8). No other clearly distinguishable morphological changes were detected. These observations demonstrate friction-induced surface modification but do not provide a quantitative measure of material removal. Accordingly, the SEM images are interpreted qualitatively and are not used to rank the wear resistance of the investigated configurations.

Quantitative contact profilometry did not provide reliable sliding-track dimensions because the compliant TPU surface deformed under the stylus and the amplitude of the rough as-printed topography was comparable to the residual track relief. Optical microscopy was likewise unsuitable for quantitative depth determination because the transparency of TPU prevented unambiguous identification of the surface boundary and track edges. Wear depth, track area and wear volume could not be calculated.

The differences in hardness and COF between GI-1 and GI-2 are consistent with the contrasting subsurface support of the two architectures. As discussed above, however, the present data do not establish a unique friction mechanism or provide independent structural validation.

3.6. Comparative Assessment of Infill Architectures and Recommendations for Their Application

With uniform infill, increasing the infill density simultaneously affects part mass, tensile and compressive resistance, and the contact compliance of the outer shell [20–23]. Stepwise redistribution of the infill, by contrast, provides greater flexibility in tailoring bulk and contact properties without changing the external geometry or material composition of the part.

From an engineering perspective, the investigated architectures can be interpreted as follows. The uniform 50%, 70% and 90% configurations provide a predictable range of properties, from the lightest and most compliant to the densest and stiffest. The gradient configurations, however, produce distinct combinations of bulk and surface properties:

- GI-1 combined a hardness comparable to that of the uniform 90% configuration, the lowest COF among all investigated architectures, and lower compressive stresses at 20% strain than the uniform 70% and 90% specimens.

- GI-2, whose mean experimental density did not differ significantly from that of the uniform 70% configuration, combined higher mean tensile strength, elongation at break, and work of deformation to failure with a hardness similar to that of the uniform 50% configuration.

On the basis of these results, GI-1 may be suitable for components that require greater resistance of the outer shell to local indentation while retaining bulk compressive compliance. GI-2 may be appropriate for applications that need lower surface hardness together with high deformation-energy absorption, such as damping and shock-absorbing elements. Potential applications include dynamic seals, elastic supports and protective pads for GI-1, and shock-absorbing inserts, footwear components, and orthotic parts for GI-2. These suggestions are based on monotonic mechanical testing and short-duration tribological testing. Application-specific validation under cyclic loading, creep and long-term sliding is still required.

The main characteristics and potential applications of the investigated configurations are summarized in Table 5. Both gradient architectures were fabricated on a standard single-extruder FFF printer using Ultimaker Cura modifiers, without multi-material printing or additional post-processing. Infill distribution can be treated as an additional design variable, alongside overall density, perimeter count and shell thickness.

Table 5. Comparative characteristics and potential application areas of the investigated infill architectures.

Architecture	Primary Combination of Characteristics	Intended Function/Design Intent	Potential Applications
Uniform 50% infill	Low density and hardness, high compliance	Weight reduction with moderate load-bearing requirements	Lightweight flexible components
Uniform 70% infill	Intermediate bulk and surface properties	General-purpose balance of density, stiffness, and compliance	General-purpose flexible components
Uniform 90% infill	High density, hardness, and compressive resistance	Enhanced bulk stiffness and load-bearing capacity	Load-bearing flexible components requiring relatively high stiffness
GI-1	High surface hardness, low COF, and enhanced bulk compressive compliance	Combination of high surface hardness and bulk compliance	Dynamic seals, elastic supports, and protective pads
GI-2	Lower surface hardness and high deformation energy absorption at moderate density	Combination of a compliant surface response, high tensile deformability, and a dense load-bearing core	Shock-absorbing inserts, damping pads, footwear components, and orthotic parts

Overall, the specific-property data demonstrate that the gradient configurations showed higher specific tensile properties than the uniform counterparts.

Direct quantitative comparison with the existing literature is challenging because of differences in materials, printing conditions and testing methodologies [8,17,21]. Nevertheless, these findings are qualitatively consistent with earlier observations on graded TPU structures [21,22] while extending them in several respects: (1) the use of discrete step-gradients rather than continuous density variations; (2) the combined analysis of mechanical, contact and friction properties; and (3) the assessment of material efficiency through specific properties (σ_{sp}, W_{sp}). These points distinguish the study from earlier graded-TPU work and show the engineering potential of step-gradient infill architectures for FFF-printed TPU components.

The contributions of spatial architecture and total material content could not be fully decoupled here because the two gradient configurations differed in both the arrange-

ment and the volumetric proportions of their local infill zones. This limitation should be addressed in future work through matched-density experimental designs. The most direct comparison is therefore that between GI-2 and the uniform 70% configuration, the only pair with no statistically significant density difference. Future investigations should examine not only symmetric step-gradient architectures but also linear and asymmetric gradient profiles. Such gradients should be designed with matched nominal mean infill densities and subsequently verified to show no statistically significant difference in experimental density, thereby allowing the effect of spatial material distribution to be isolated more rigorously.

4. Conclusions

Spatial distribution of triangular infill is an effective design variable for FFF-printed TPU 95A: it changes bulk tensile and compressive behavior and the contact response of the outer shell without a change in external geometry. The main conclusions are as follows.

1. After normalization to experimental density, both gradient architectures showed higher specific tensile strength and specific work of deformation to failure than the uniform infills. The most direct comparison is GI-2 versus the uniform 70% configuration. No statistically significant difference was detected between their mean experimental densities (0.988 vs. 0.990 g/cm^3), yet GI-2 had significantly higher tensile strength (20.3 vs. 18.4 MPa) and work of deformation to failure (48.3 vs. 32.3 MJ/m^3). GI-1 reached 21.5 MPa and 45.6 MJ/m^3, above the uniform 90% values (20.1 MPa and 32.7 MJ/m^3), but GI-1 was also less dense (1.028 vs. 1.090 g/cm^3), so architecture and material content are confounded in that pair.

2. The gradient specimens combined high tensile extensibility (about 349–354%) with greater compressive compliance. Mean compressive stresses at 20% strain were lower than those of the uniform 70% and 90% specimens. This combination may be useful where both tensile energy absorption and a compliant compressive response are required, but it still requires validation in application-specific geometries.

3. Shore D hardness followed the subsurface infill rather than the mean density. The hardness of GI-1 (49.2) did not differ significantly from that of the uniform 90% configuration, whereas the hardness of GI-2 did not differ significantly from that of the uniform 50% configuration. This indicates that the solid outer shell and the underlying infill acted as a mechanically coupled system.

4. GI-1 gave the lowest mean COF over 250–300 m (0.50 ± 0.01). The result is consistent with lower contact compliance of the surface-dense architecture, but it does not identify a single friction mechanism. With $n = 3$ specimens per configuration and no quantitative wear data, the frictional results are descriptive and should not be used to rank wear resistance.

Gradient order and total material content could not be isolated because GI-1 and GI-2 differed in nominal mean infill density. Future work should use density-matched gradient designs, direct three-dimensional checks of the printed infill, local strain mapping, cyclic and creep testing, contact-indentation measurements under the tribological load, and quantitative wear analysis.

Supplementary Materials: The following supporting information can be downloaded at: https://www.mdpi.com/article/10.3390/technologies14090536/s1, Figure S1: Representative tensile stress–strain curves for TPU 95A specimens with uniform and step-gradient infill architectures; Table S1: Individual tensile strength, elongation at break, and work of deformation to failure values for TPU 95A specimens with uniform and step-gradient infill architectures; Table S2: Descriptive and inferential statistical analysis of the tensile properties of TPU 95A specimens with uniform and step-gradient infill architectures; Table S3: Individual compressive stress values at relative strains of 5 %, 10 %, and 20 % for TPU 95A specimens with uniform and step-gradient infill architectures;

Table S4: Descriptive and inferential statistical analysis of compressive stress at 5 %, 10 %, and 20 % strain for TPU 95A specimens with uniform and step-gradient infill architectures; Table S5: Individual Shore D hardness values for TPU 95A specimens with uniform and step-gradient infill architectures; Table S6: Descriptive and inferential statistical analysis of Shore D hardness for TPU 95A specimens with uniform and step-gradient infill architectures; Table S7: Individual experimental density values and descriptive statistics for TPU 95A specimens with uniform and step-gradient infill architectures; Table S8: One-way ANOVA results for the experimental density of TPU 95A specimens; Table S9: Tukey's HSD pairwise comparisons of experimental density among the investigated infill configurations; Table S10: Individual specimen-level mean COF values calculated over the 250–300 m sliding-distance interval; Data S1: Raw tensile stress–strain curves for all individual specimens (wide format, CSV); Data S2: Raw compression stress–strain curves for all individual specimens (wide format, CSV).

Author Contributions: Conceptualization, A.P.V.; methodology, A.P.V. and A.A.O.; software, A.P.V., I.S.M. and A.A.O.; validation, A.P.V., I.S.M. and A.A.O.; formal analysis, A.P.V.; investigation, A.P.V. and I.S.M.; resources, I.S.M.; data curation, A.P.V. and I.S.M.; writing—original draft preparation, A.P.V. and A.A.O.; writing—review and editing, A.P.V. and A.A.O.; visualization, A.P.V. and I.S.M.; supervision, A.P.V. and A.A.O.; project administration, A.P.V.; funding acquisition, A.P.V. All authors have read and agreed to the published version of the manuscript.

Funding: This research was funded by the Russian Science Foundation, grant number 25-23-01017, https://rscf.ru/project/25-23-01017/ (accessed on 25 July 2026).

Institutional Review Board Statement: Not applicable.

Informed Consent Statement: Not applicable.

Data Availability Statement: The data supporting the findings of this study are available within the article and its Supplementary Materials.

Conflicts of Interest: The authors declare no conflicts of interest.

Abbreviations

The following abbreviations are used in this manuscript:

COF	Coefficient of Friction
DSC	Differential Scanning Calorimetry
FFF	Fused Filament Fabrication
FTIR	Fourier-Transform Infrared Spectroscopy
GI-1	Gradient Infill 1 (Surface-dense configuration: 90–70–50–70–90%)
GI-2	Gradient Infill 2 (Core-dense configuration: 50–70–90–70–50%)
SEM	Scanning Electron Microscopy
TPU	Thermoplastic Polyurethane

References

1. Ben Said, L.; Ayadi, B.; Alharbi, S.; Dammak, F. Recent Advances in Additive Manufacturing: A Review of Current Developments and Future Directions. *Machines* **2025**, *13*, 813. [CrossRef]
2. Desai, S.M.; Sonawane, R.Y.; More, A.P. Thermoplastic Polyurethane for Three-dimensional Printing Applications: A Review. *Polym. Adv. Techs* **2023**, *34*, 2061–2082. [CrossRef]
3. Alarifi, I.M. A Comprehensive Review on Advancements of Elastomers for Engineering Applications. *Adv. Ind. Eng. Polym. Res.* **2023**, *6*, 451–464. [CrossRef]
4. Marco, V.; Massimo, G.; Manuela, G. Additive Manufacturing of Flexible Thermoplastic Polyurethane (TPU): Enhancing the Material Elongation through Process Optimisation. *Prog. Addit. Manuf.* **2025**, *10*, 2877–2891. [CrossRef]
5. Shin, E.J.; Prasad, C.; Choi, H.Y. Recent Advances in Thermoplastic Polyurethane-Based Composites, Properties, Synthesis and Its Applications. *J. Ind. Eng. Chem.* **2026**, *156*, 150–191. [CrossRef]
6. Xiang, N.; Zhang, X.; Zheng, M.; Xu, R.; Yan, Y. Investigation of Tensile Behavior and Molecular Structure of the Thermoplastic Polyurethane Sheets Injection Molded at Different Mold Temperatures. *J. Appl. Polym. Sci.* **2021**, *138*, 50959. [CrossRef]

7. Cavender-Word, T.J.; Roberson, D.A. Development of a Resilience Parameter for 3D-Printable Shape Memory Polymer Blends. *Materials* **2023**, *16*, 5906. [CrossRef] [PubMed]
8. Levin, D.Y.; Boldyrev, A.I.; Podshibyakin, M.E.; Riabinina, O.A. Tensile Properties of Thermoplastic Materials Produced by FDM: PLA+, TPU E95A, and TPU 60D CFF. *Ipolytech J.* **2026**, *30*, 19–33, (In Russ.). [CrossRef]
9. Ansari, A.A.; Kamil, M. Effect of Print Speed and Extrusion Temperature on Properties of 3D Printed PLA Using Fused Deposition Modeling Process. *Mater. Today Proc.* **2021**, *45*, 5462–5468. [CrossRef]
10. Sardinha, M.; Ferreira, L.; Diogo, H.; Ramos, T.R.P.; Reis, L.; Vaz, M.F. Material Extrusion of TPU: Thermal Characterization and Effects of Infill and Extrusion Temperature on Voids, Tensile Strength and Compressive Properties. *Rapid Prototyp. J.* **2025**, *31*, 62–81. [CrossRef]
11. Le, D.; Nguyen, C.H.; Pham, T.H.N.; Nguyen, V.T.; Pham, S.M.; Le, M.T.; Nguyen, T.T. Optimizing 3D Printing Process Parameters for the Tensile Strength of Thermoplastic Polyurethane Plastic. *J. Mater. Eng. Perform.* **2023**, *32*, 10805–10816. [CrossRef]
12. Albardawil, A.; Aditya, A.R.M.; Mubarok, M.Y.; Islami, L.A.; Mardiyana, D. Improving the Mechanical Performance of TPU95A Filament in FDM 3D Printing via Parameter Optimization Using the Taguchi Method. *Eng. Proc.* **2025**, *107*, 62. [CrossRef]
13. Bruère, V.M.; Lion, A.; Holtmannspötter, J.; Johlitz, M. The Influence of Printing Parameters on the Mechanical Properties of 3D Printed TPU-Based Elastomers. *Prog. Addit. Manuf.* **2023**, *8*, 693–701. [CrossRef]
14. Amorim, D.J.N.; Nachtigall, T.; Alonso, M.B. Exploring Mechanical Meta-Material Structures through Personalised Shoe Sole Design. In *Proceedings of the ACM Symposium on Computational Fabrication*; ACM: Pittsburgh, PA, USA, 2009; pp. 1–8. [CrossRef]
15. Wang, Y.; Ren, X.; Chen, Z.; Jiang, Y.; Cao, X.; Fang, S.; Zhao, T.; Li, Y.; Fang, D. Numerical and Experimental Studies on Compressive Behavior of Gyroid Lattice Cylindrical Shells. *Mater. Des.* **2020**, *186*, 108340. [CrossRef]
16. Brăileanu, P.I.; Mocanu, M.-T.; Dobrescu, T.G.; Dobrotă, D.; Pascu, N.E. Structure—Property—Performance Relationships in Thermoplastic Polyurethane: Influence of Infill Density and Surface Texture. *Polymers* **2025**, *17*, 2716. [CrossRef] [PubMed]
17. Rodríguez-Parada, L.; De La Rosa, S.; Mayuet, P.F. Influence of 3D-Printed TPU Properties for the Design of Elastic Products. *Polymers* **2021**, *13*, 2519. [CrossRef] [PubMed]
18. Nace, S.E.; Tiernan, J.; Holland, D.; Ni Annaidh, A.A. Comparative Analysis of the Compression Characteristics of a Thermoplastic Polyurethane 3D Printed in Four Infill Patterns for Comfort Applications. *Rapid Prototyp. J.* **2021**, *27*, 24–36. [CrossRef]
19. Jung, I.; Lee, S. Compressive properties of 3D printed TPU samples. *J. Korean Soc. Cloth. Text.* **2022**, *46*, 481–493. [CrossRef]
20. Garrido Silva, B.; Alves, F.; Sardinha, M.; Reis, L.; Leite, M.; Deus, A.M.; Vaz, M.F. Functionally Graded Cellular Cores of Sandwich Panels Fabricated by Additive Manufacturing. *Proc. Inst. Mech. Eng. Part L J. Mater. Des. Appl.* **2022**, *236*, 1814–1828. [CrossRef]
21. Bates, S.R.G.; Farrow, I.R.; Trask, R.S. Compressive Behaviour of 3D Printed Thermoplastic Polyurethane Honeycombs with Graded Densities. *Mater. Des.* **2019**, *162*, 130–142. [CrossRef]
22. Płatek, P.; Rajkowski, K.; Cieplak, K.; Sarzyński, M.; Małachowski, J.; Woźniak, R.; Janiszewski, J. Deformation Process of 3D Printed Structures Made from Flexible Material with Different Values of Relative Density. *Polymers* **2020**, *12*, 2120. [CrossRef] [PubMed]
23. Dey, A.; Ramoni, M.; Yodo, N. A Survey on Fused Filament Fabrication to Produce Functionally Gradient Materials. *Materials* **2024**, *17*, 3675. [CrossRef] [PubMed]
24. Aslan, E.; Akincioğlu, G. Tribological Characterization of Two Different Elastic Polymers Produced via FDM. In *Proceedings of the International Symposium on Lightweight and Sustainable Polymeric Materials (LSPM23)*; Mavinkere Rangappa, S., Siengchin, S., Eds.; Springer Proceedings in Materials; Springer Nature: Singapore, 2023; Volume 32, pp. 189–200. [CrossRef]
25. Garg, N.; Kumar, P. Multi-Objective Optimization of 3D Printing Parameters to Fabricate TPU for Tribological Applications. *Proc. Inst. Mech. Eng. Part E J. Process Mech. Eng.* **2026**, *240*, 3281–3292. [CrossRef]
26. Hossain, K.R.; Lyu, Y.; Yao, X.; Yang, Y.; Jiang, P.; Wang, X. Tribological and Mechanical Properties of Fabricated Soft Materials with a Podium Mesostructured. *Tribol. Int.* **2023**, *187*, 108673. [CrossRef]
27. Aslan, E.; Akıncıoğlu, G. Investigation of the Wear and Friction Profile of TPU-Based Polymers at Different Infill Ratios. *Int. J. Automot. Sci. Technol.* **2024**, *8*, 125–131. [CrossRef]
28. *ISO 291:2008*; Plastics—Standard Atmospheres for Conditioning and Testing. ISO: Geneva, Switzerland, 2008.
29. *ASTM D638-22*; Standard Test Method for Tensile Properties of Plastics. ASTM International: West Conshohocken, PA, USA, 2022.
30. *ASTM D695-23*; Standard Test Method for Compressive Properties of Rigid Plastics. ASTM International: West Conshohocken, PA, USA, 2023.
31. *GOST 15139-69*; Plastics—Methods for the Determination of Density (Mass Density). State Committee of the Ussr for Standards: Moscow, Russia, 1969.
32. *ISO 868:2003*; Plastics and Ebonite—Determination of Indentation Hardness by Means of a Durometer (Shore Hardness). ISO: Geneva, Switzerland, 2003.
33. Sotov, A.; Abdrakhmanova, A.; Zaytsev, A.; Popovich, A. Additive Manufacturing of Functional Gradient Thermoplastic Composite Using Fused Deposition Modelling and Coextrusion Continuous Fibres. *Int. J. Adv. Manuf. Technol.* **2025**, *137*, 3587–3601. [CrossRef]

34. León-Calero, M.; Reyburn Valés, S.C.; Marcos-Fernández, Á.; Rodríguez-Hernandez, J. 3D Printing of Thermoplastic Elastomers: Role of the Chemical Composition and Printing Parameters in the Production of Parts with Controlled Energy Absorption and Damping Capacity. *Polymers* **2021**, *13*, 3551. [CrossRef] [PubMed]
35. Eyri, B.; Gul, O.; Karsli, N.G.; Yilmaz, T. Study of the Thermal and Hydrothermal Aging Effects on the Properties of 3D-Printed Thermoplastic Polyurethane. *Vinyl Addit. Technol.* **2025**, *32*, 889–902. [CrossRef]
36. Xiao, J.; Gao, Y. The Manufacture of 3D Printing of Medical Grade TPU. *Prog. Addit. Manuf.* **2017**, *2*, 117–123. [CrossRef]
37. Kim, M.; Lee, S. Modeling and Development of Continuous Textile Structures Utilizing 3D Printing. *Fash. Text.* **2025**, *12*, 34. [CrossRef]
38. Shin, E.J.; Jung, Y.S.; Park, C.H.; Lee, S. Eco-Friendly TPU/PLA Blends for Application as Shape-Memory 3D Printing Filaments. *J. Polym. Environ.* **2023**, *31*, 3182–3196. [CrossRef]
39. Wu, C.-H.; Huang, Y.-C.; Chen, W.-L.; Lin, Y.-Y.; Dai, S.A.; Tung, S.-H.; Jeng, R.-J. Size-Dependent Phase Separation and Thermomechanical Properties of Thermoplastic Polyurethanes. *Polymer* **2020**, *210*, 123075. [CrossRef]
40. Dos Santos, A.N.; Pesce, M.; Ceseracciu, L.; Nardi, M.; Vasile, F.; Falletta, E.; Chiolerio, A. Robust, Self-Healing Polyurea/TPU Elastomers. *Polym. Test.* **2026**, *160*, 109209. [CrossRef]
41. Gorbunova, M.A.; Komov, E.V.; Grunin, L.Y.; Ivanova, M.S.; Abukaev, A.F.; Imamutdinova, A.M.; Ivanov, D.A.; Anokhin, D.V. The Effect of Separation of Blocks on the Crystallization Kinetics and Phase Composition of Poly(Butylene Adipate) in Multi-Block Thermoplastic Polyurethanes. *Phys. Chem. Chem. Phys.* **2022**, *24*, 902–913. [CrossRef] [PubMed]
42. Bruckmoser, K.; Resch, K. Investigation of Ageing Mechanisms in Thermoplastic Polyurethanes by Means of IR and Raman Spectroscopy. *Macromol. Symp.* **2014**, *339*, 70–83. [CrossRef]
43. Redel, M.; Regelmann, C.; Wölfel, B.; Schubert, D.W. Analysis of Morphology Changes in Thermoplastic Polyurethane During Storage and Processing Using FTIR Spectroscopy. *Adv. Polym. Technol.* **2026**, *2026*, 3883260. [CrossRef]
44. Sun, X.; Mazur, M.; Cheng, C.-T. A Review of Void Reduction Strategies in Material Extrusion-Based Additive Manufacturing. *Addit. Manuf.* **2023**, *67*, 103463. [CrossRef]
45. Sepahi, M.T.; Abusalma, H.; Jovanovic, V.; Eisazadeh, H. Mechanical Properties of 3D-Printed Parts Made of Polyethylene Terephthalate Glycol. *J. Mater. Eng. Perform.* **2021**, *30*, 6851–6861. [CrossRef]
46. Gonabadi, H.; Yadav, A.; Bull, S.J. The Effect of Processing Parameters on the Mechanical Characteristics of PLA Produced by a 3D FFF Printer. *Int. J. Adv. Manuf. Technol.* **2020**, *111*, 695–709. [CrossRef]
47. Broitman, E. Indentation Hardness Measurements at Macro-, Micro-, and Nanoscale: A Critical Overview. *Tribol. Lett.* **2017**, *65*, 23. [CrossRef]
48. Hakami, F.; Pramanik, A.; Basak, A.K. *Tribology of Elastomers*; SpringerBriefs in Applied Sciences and Technology; Springer Nature: Singapore, 2022; ISBN 978-981-19-2907-6. [CrossRef]
49. Tockner, M.; Stiller, T.; Staudinger, P.; Fasching, M.; Pondicherry, K.; Hausberger, A.; Grün, F.; Schwarz, T. Fretting Behavior of TPU under Sub-Ambient to Elevated Temperatures: Development of a Novel High-Resolution, High-Frequency, Low-Amplitude Test Method for Sealing Materials. *Wear* **2026**, *586*, 206442. [CrossRef]
50. Brăileanu, P.I.; Mocanu, M.-T.; Pascu, N.E. Tribological Assessment of FFF-Printed TPU Under Dry Sliding Conditions for Sustainable Mobility Components. *Future Transp.* **2025**, *5*, 184. [CrossRef]

Disclaimer/Publisher's Note: The statements, opinions and data contained in all publications are solely those of the individual author(s) and contributor(s) and not of MDPI and/or the editor(s). MDPI and/or the editor(s) disclaim responsibility for any injury to people or property resulting from any ideas, methods, instructions or products referred to in the content.